Coherence, alignment and fibre-profile geometry in a hierarchical texture-descriptor tensor: application to H&E sections of skeletal muscle in wild boar (*Sus scrofa*) and domestic pigs

Ştefan Ţălu

The Directorate of Research, Development and Innovation Management (DMCDI), The Technical University of Cluj-Napoca, Cluj-Napoca, Romania. Corresponding author: Ş. Ţălu, stefan.talu@auto.utcluj.ro

https://doi.org/10.67784/0098

Abstract. Muscle fibre size, shape and the organisation of intramuscular connective tissue are central to pork quality, but histological sections are usually summarised by fibre counts and diameters, which require segmentation and ignore direction. This study extends a hierarchical texture-descriptor tensor (channel × scale × orientation × region of interest, ROI) with three results that decompose its anisotropy index *A*: (1) an exact factorisation of *A* into energy-weighted local coherence and alignment of local axes, which trade off monotonically with the integration scale and cross at $\sqrt{A}$ (for 0 < A < 1); (2) an exact decomposition of A over tissue compartments of arbitrary area, from which a two-compartment cancellation law and a dilution law follow; and (3) a closed-form boundary-profile law giving the anisotropy produced by elliptical fibre profiles of aspect ratio *a* in terms of complete elliptic integrals. The tensor (10 channels, 4 scales, 4 orientations; 1 and 4 ROIs) was applied to eight published, calibrated haematoxylin-eosin images of *longissimus dorsi* and *biceps femoris*: four of wild boar (three transverse, one longitudinal) and two magnifications each of Xiang and Large White pigs. The boundary-profile law was reproduced on synthetic ellipses within 0.003 and on synthetic mosaics within 0.004. All eight sections were anisotropic relative to isotropic surrogates ($P \leq 0.005$ at $s = 2$ px), with *A* from 0.019 (Large White, detail) to 0.697 (wild boar, longitudinal; texture axis 90.8°, along the fibres). The interfibre band carried 0.83–0.93 of the gradient energy on 0.24–0.50 of the area; where wide perimysial septa were present they dominated *A*, and in the Large White detail field septal and endomysial contributions with nearly perpendicular axes cancelled, reducing *A* by 90 %. At the fascicle scale (s = 22 µm) the Large White overview was strongly anisotropic and the Xiang overview was not (*A* = 0.480 versus 0.071, non-overlapping intervals), and the characteristic scale of Xiang muscle agreed across magnifications (13.5 and 13.6 µm), whereas that of Large White did not (15.9 and 5.2 µm). Median minor-axis lengths of segmented fibres were 42.4 µm (Xiang, detail) and 61.6 µm (Large White, overview), close to the diameters reported by the source study, but the other two fields gave 53.5 and 53.3 µm, so agreement depended on the field. The results show that the tensor separates fibre-level and fascicle-level organisation of porcine muscle; the tensor itself requires no segmentation, whereas the compartment and fibre-profile analyses do; breed or quality differences are not claimed from single published images.

Key Words: *longissimus dorsi*, muscle histology, texture analysis, structure tensor, anisotropy, perimysium, intramuscular connective tissue, meat quality.

Introduction. The histological architecture of porcine skeletal muscle is one of the main determinants of meat quality. Fibre number, cross-sectional area and type composition are related to growth, *post-mortem* metabolism, colour, water-holding capacity and tenderness (Karlsson et al., 1999; Ryu & Kim, 2005; Lefaucheur, 2010; Joo et al., 2013), and the intramuscular connective tissue that groups fibres into fascicles (endomysium, perimysium) and the intramuscular fat deposited in it contribute to texture and eating quality (Purslow, 2005; Nishimura, 2010; Hocquette et al., 2010). Selection for lean growth has increased fibre size in commercial breeds (Rehfeldt et al., 2000), and wild and domestic pigs differ in fibre size and in the proportion of oxidative fibres (Ruusunen

& Puolanne, 2004; Cadar, 2011). Indigenous breeds such as the Chinese Xiang pig, with high intramuscular fat and small fibres, are studied as contrasts to lean Western breeds (Wang et al., 2024).

In practice these sections are described by counts and diameters of segmented fibres, or qualitatively. Segmentation fails where fibres touch or where staining is uneven, and neither counts nor diameters describe direction: whether fibre profiles are elongated in a common direction, whether the connective-tissue septa are straight and parallel or branch in several directions, and at which scale these patterns appear. Texture analysis describes the image without segmentation (Haralick et al., 1973; Ţălu, 2012b; Depeursinge, 2017; Ghalati et al., 2022), and fractal, multifractal and lacunarity descriptors have been used for biological and medical images (Ţălu & Giovanzana, 2011, 2012; Ţălu, 2012a, 2013a, 2013b; Ţălu et al., 2013, 2015) and in aquaculture (Petrescu-Mag et al., 2026), but scalar descriptors do not identify a preferred direction or the tissue component that produces it.

A hierarchical texture-descriptor tensor that keeps scale, orientation and region as separate indices was introduced for this purpose and applied to human and fish skeletal muscle (Ţălu, 2027a) and to guppy muscle (Ţălu, 2026c), and has also been used for myostatin-edited rabbit muscle (Ţălu, 2027b) and for soil thin sections (Ţălu, 2027c). In those studies the directional-energy block of the tensor was shown to be a quadratic form of the regional structure matrix, which defines an anisotropy index *A* and a texture axis ψ exactly from four orientations, and pooling equal-area regions was shown to lower *A*. What remained open is what *A* is made of. A given value of *A* can arise from weak local order that is well aligned, or from strong local order whose direction varies across the section; it can be produced by fibre outlines, by connective-tissue septa or by both; and it depends on the shape of the fibre profiles, which in turn depends on how obliquely the fibres were cut.

The present study answers these questions with three new results (Section 2) and applies them to porcine muscle. Proposition 1 factorises *A* into local coherence and alignment of local axes as a function of the integration scale. Proposition 2 decomposes *A* exactly over tissue compartments of arbitrary area (septa, endomysium, fibre interiors, adipocytes). Proposition 3 gives in closed form the anisotropy produced by elliptical fibre profiles, which links *A* to fibre shape and section obliquity. The tensor and the three results were applied to eight published haematoxylin-eosin (H&E) images with scale bars: four of wild boar muscle (Odung et al., 2025) and two magnifications each of the *longissimus dorsi* of Xiang and Large White pigs (Wang et al., 2024). The aims were to verify the new results on synthetic and real images, to identify which tissue components produce directional organisation at each scale, and to compare the readings with the morphometry reported by the source studies, as a step towards the measurement-based frameworks proposed for translational human and veterinary medicine (Ţălu, 2026a, 2026b). Diagnostic or breed-classification performance is not evaluated.

Theoretical Framework

Descriptor tensor and anisotropy index. Let $f(\mathbf{x})$ be the luminance of an H&E image, standardised to zero mean and unit variance, and $G_s = g_s * f$ its Gaussian scale-space at scale *s* (Lindeberg, 1998). With $\mathbf{u}_\theta = (\cos\theta, \sin\theta)^{\mathrm{T}}$ (θ counter-clockwise from the image rows, *y* axis upward), the steerable directional derivatives are (Freeman & Adelson, 1991)

$$\partial_\theta G_s = \mathbf{u}_\theta \cdot \nabla G_s, \qquad \partial_\theta^2 G_s = \mathbf{u}_\theta^{\mathrm{T}} \nabla\nabla^{\mathrm{T}} G_s \, \mathbf{u}_\theta \qquad (1)$$

and for regions $\Omega_1, \ldots, \Omega_R$ each channel *m* summarises a local response over a region, giving the fourth-order array

$$\mathfrak{D} \in \mathbb{R}^{M\times K\times L\times R}, \qquad \mathfrak{D}_{mklr} = D_m(s_k, \theta_l, \Omega_r) \qquad (2)$$

with *M* = 10 channels (Table 1), *K* = 4 scales (*s* = 1, 2, 4, 8 px), *L* = 4 orientations (θ = 0, π/4, π/2, 3π/4) and *R* = 1 or 4 ROIs (160 or 640 entries). The configuration is the same as in Ţălu (2027a), so that values can be compared. For the directional energy $D_2 = \langle(\partial_\theta G_s)^2\rangle_r$, Proposition 1 of that study gives $D_2(\theta) = \mathbf{u}_\theta^{\mathrm{T}}\mathbf{J}\mathbf{u}_\theta$, where $\mathbf{J} = \langle\nabla G_s \nabla G_s^{\mathrm{T}}\rangle_r$ is the

regional structure matrix (Bigün & Granlund, 1987), and the anisotropy index and texture axis are

$$A = \frac{\lambda_+ - \lambda_-}{\lambda_+ + \lambda_-} = \frac{|\langle z \rangle|}{\langle |z| \rangle}, \qquad z = \left(\partial_x G_s + i\ \partial_y G_s\right)^2, \qquad \psi = 1/2 \arg\langle z \rangle + \pi/2 \ (\mathrm{mod}\ \pi) \qquad (3)$$

where $\lambda_\pm$ are the eigenvalues of **J** and $|z| = |\nabla G_s|^2$. The doubled-angle form in (3) (Mardia & Jupp, 2000) is the starting point of the three results below. In a transverse section gradients are perpendicular to fibre outlines and septa, so ψ is the direction along which these boundaries run, and *A* measures how consistently they share it.

Table 1

Channels of the descriptor tensor. All channels are evaluated for every $(s_k, \theta_l, \Omega_r)$; $\langle\cdot\rangle_r$ is the mean over Ω_r.

Channel	*Definition*	*Type*
D1	$\langle \lvert\partial_\theta G_s\rvert \rangle_r$	Gradient amplitude
D2	$\langle (\partial_\theta G_s)^2 \rangle_r$	Directional energy
D3	Kurtosis of $\partial_\theta G_s$ over Ω_r	Distribution shape
D4	Shannon entropy of $\partial_\theta G_s$ (32 bins over ±4 SD, bits)	Distribution shape
D5	$\langle \lvert\partial_\theta^2 G_s\rvert \rangle_r$	Second-derivative amplitude
D6–D9	GLCM contrast, homogeneity, energy, correlation of G_s (16 levels; symmetric offsets ±*d*, *d* = *s* along θ)	Co-occurrence (Haralick et al., 1973)
D10	Normalised autocorrelation of G_s at lag 2*s* along ±θ	Spatial correlation

Local coherence and alignment (Proposition 1). Replacing the pixel tensor $\nabla G_s \nabla G_s^{\mathrm{T}}$ by its Gaussian-weighted local mean of width ρ gives the structure-tensor field $\mathbf{J}_\rho(\mathbf{x})$, with energy $w_\rho = \mathrm{tr}\mathbf{J}_\rho$, local coherence $\kappa_\rho = (\lambda_+ - \lambda_-)/(\lambda_+ + \lambda_-)$ and local orientation φ_ρ; in complex form $z_\rho = \left(J_{\rho,xx} - J_{\rho,yy}\right) + 2iJ_{\rho,xy} = \kappa_\rho w_\rho e^{2i\varphi_\rho}$, and $z_0 = z$. For a region Ω define the energy-weighted mean coherence and the resultant length of the local axes,

$$\bar{\kappa}_E(\rho) = \frac{\sum_\Omega \kappa_\rho\, w_\rho}{\sum_\Omega w_\rho}, \qquad R(\rho) = \frac{\left|\sum_\Omega \kappa_\rho\, w_\rho e^{2i\varphi_\rho}\right|}{\sum_\Omega \kappa_\rho\, w_\rho}, \qquad A_\rho = \frac{\left|\sum_\Omega z_\rho\right|}{\sum_\Omega w_\rho} \qquad (4)$$

Proposition 1 (coherence–alignment factorisation). (i) For every ρ and every region, $A_\rho = \bar{\kappa}_E(\rho)\, R(\rho)$. (ii) If the smoothing preserves sums over Ω (periodic domain, or Ω the whole support), then $A_\rho = A$ for all ρ, $\bar{\kappa}_E$ is non-increasing and *R* non-decreasing in ρ, with $\bar{\kappa}_E(0) = 1$, $R(0) = A$ and $\bar{\kappa}_E \to A$, $R \to 1$ as ρ → ∞ (the last limit for A > 0). Consequently, for 0 < A < 1, there is an integration scale ρ_c at which

$$\bar{\kappa}_E(\rho_c) = R(\rho_c) = \sqrt{A} \qquad (5)$$

Proof. (i) $|z_\rho| = \kappa_\rho w_\rho$, so $\bar{\kappa}_E R = |\sum z_\rho| / \sum w_\rho$. (ii) Convolution with a normalised kernel preserves $\sum w_\rho$ and $\sum z_\rho$, hence $A_\rho = A_0 = A$. Because Gaussian kernels form a semigroup, $z_{\rho_2} = h * z_{\rho_1}$ with $h = g_{\sqrt{\rho_2^2 - \rho_1^2}}$ for $\rho_2 > \rho_1$, and the triangle inequality gives $|z_{\rho_2}(\mathbf{x})| \le \sum_{\mathbf{y}} h(\mathbf{x} - \mathbf{y}) |z_{\rho_1}(\mathbf{y})|$; summing over **x**, $\sum |z_{\rho_2}| \le \sum |z_{\rho_1}|$, so $\bar{\kappa}_E$ does not increase and $R = A/\bar{\kappa}_E$ does not decrease. At ρ = 0 the pixel tensor has rank one, so $\kappa_0 = 1$ wherever $w_0 > 0$; as ρ → ∞, z_ρ tends to its mean and $\bar{\kappa}_E \to A$. Continuity gives (5).

The limiting cases are excluded from (5): for A = 1 all local axes coincide and $\bar{\kappa}_E$ = R = 1 for every ρ, whereas for A = 0 the numerator and the denominator of R both vanish as ρ → ∞, so that R has no limit and no crossover is defined. Proposition 1 separates two reasons why A can be low: local disorder (low $\bar{\kappa}_E$ at small ρ) and disagreement between well-ordered domains (low *R*). Their product is fixed, so making the local window larger converts local order into alignment without changing *A*. The crossover scale ρ_c is the window at which local order and alignment contribute equally; it is an orientation-domain size, which can be compared with fibre diameter and fascicle size. On a finite ROI with reflective boundaries, part (ii) holds only approximately; the deviation of A_ρ from *A* is reported.

Tissue compartments (Proposition 2). Let $\Omega = \bigcup_c \Omega_c$ be a partition into compartments of *arbitrary* area (for example septa, endomysial band, fibre interiors, adipocytes), with compartment anisotropy A_c, axis ψ_c and energy share

$$\varepsilon_c = \frac{\sum_{\Omega_c} |\nabla G_s|^2}{\sum_{\Omega} |\nabla G_s|^2}, \qquad \text{then} \qquad A\, e^{2i\psi} = \sum_c \varepsilon_c\, A_c\, e^{2i\psi_c} \qquad (6)$$

Proof. By (3), $Ae^{2i(\psi-\pi/2)} = \sum_\Omega z \,/\, \sum_\Omega |z|$. Splitting the numerator over compartments and writing $\sum_{\Omega_c} z = A_c e^{2i(\psi_c-\pi/2)} \sum_{\Omega_c} |z|$ gives (6).

Three consequences are used. (a) $A \le \sum_c \varepsilon_c\, A_c$, with equality only if all compartments with $A_c > 0$ share the same axis; this generalises the equal-area pooling inequality of Ƭălu (2027a) to unequal areas and to compartments defined by tissue class. (b) For two compartments,

$$A^2 = \varepsilon_1^2 A_1^2 + \varepsilon_2^2 A_2^2 + 2\varepsilon_1\varepsilon_2 A_1 A_2 \cos 2(\psi_1 - \psi_2) \qquad (7)$$

so compartments with perpendicular axes cancel ($A = |\varepsilon_1 A_1 - \varepsilon_2 A_2|$), and a section can appear isotropic although each of its components is oriented. (c) If one compartment is isotropic ($A_i = 0$), for example randomly arranged adipocytes, then

$$A = (1 - \varepsilon_i)\, A_m \qquad (8)$$

where A_m is the anisotropy of the remaining tissue. The dilution weight is the *energy* share of the isotropic component, not its area share. Adipocyte interiors are nearly uniform and carry little gradient energy, so intramuscular fat lowers *A* through the density of adipocyte boundaries, and only when the adipocytes are numerous enough for their boundary orientations to average out.

Fibre-profile geometry (Proposition 3). Consider an image made of profiles of uniform contrast *c* (fibres on a background of different intensity), observed at a scale *s* that is small compared with the radius of curvature of the outlines and with their separation. Across an outline, $\nabla G_s \approx -c\, g_s^{(1)}(d)\, \mathbf{n}$, where *d* is the signed distance to the outline, **n** the outward normal and $g_s^{(1)}$ the one-dimensional Gaussian; since $\int g_s^{(1)}(d)^2\, \mathrm{d}d = 1/\left(2\sqrt{\pi}s\right)$, the structure matrix of one profile is $c^2\left(2\sqrt{\pi}s\right)^{-1} \oint \mathbf{n}\mathbf{n}^{\mathrm{T}}\, \mathrm{d}\ell$ up to curvature corrections of relative order *s*/(radius). For an ellipse with semi-axes α ≥ β, parametrised as $(\alpha\cos t, \beta\sin t)$, $\mathbf{n}\, \mathrm{d}\ell = (\beta\cos t, \alpha\sin t)\, \mathrm{d}t$, the off-diagonal term vanishes and

Proposition 3 (boundary-profile law). The anisotropy of an elliptical profile of aspect ratio $a = \alpha/\beta$ depends only on *a*, its texture axis is the major axis, and

$$A_{\text{shape}}(a) = \frac{(2-m)\,E(m) - 2(1-m)\,K(m)}{m\,E(m)}, \qquad m = 1 - a^{-2} \qquad (9)$$

where *K* and *E* are the complete elliptic integrals of the first and second kind with parameter *m* (Abramowitz & Stegun, 1964). For a population of profiles with perimeters P_j, aspect ratios a_j and major-axis angles θ_j,

$$A_{\text{bnd}}\, e^{2i\psi_{\text{bnd}}} = \frac{\sum_j P_j\; A_{\text{shape}}(a_j)\, e^{2i\theta_j}}{\sum_j P_j} \qquad (10)$$

Proof. With β = 1, $J_{xx} = \int_0^{2\pi} \cos^2 t/\tau\, \mathrm{d}t$ and $J_{yy} = \int_0^{2\pi} a^2 \sin^2 t/\tau\, \mathrm{d}t$, where $\tau = (\cos^2 t + a^2 \sin^2 t)^{1/2}$. Then $J_{xx} + J_{yy} = \int \tau\, \mathrm{d}t = 4aE(m)$ (the perimeter), and writing $\cos^2 t = (a^2 - \tau^2)/(a^2 - 1)$ gives $J_{xx} = 4a[K(m) - E(m)]/(a^2 - 1)$, using $\int_0^{2\pi} \tau^{-1}\, \mathrm{d}t = 4K(m)/a$. Hence $A = \left(J_{yy} - J_{xx}\right)/\left(J_{xx} + J_{yy}\right) = 1 - 2(1-m)(K-E)/(mE)$, which is (9); the leading eigenvector is along *y*, so the texture axis ψ = φ + π/2 is the major axis. Profile structure matrices add, which gives (10) by Proposition 2 applied to the outlines.

A_{shape} increases from 0 (circle) to 1 ($a \to \infty$); for nearly circular profiles $A_{\text{shape}} \approx 3/8\, m \approx 3/4\, (a-1)$, and $A_{\text{shape}}(1.5) = 0.296$, $A_{\text{shape}}(2) = 0.480$ (Figure 1b). If all profiles have the same aspect ratio, (10) reduces to $A_{\text{bnd}} = R_P\, A_{\text{shape}}(a)$, with R_P the perimeter-weighted resultant length of the profile axes. A circular cylinder cut at obliquity α to its cross-section gives an ellipse with $a = \sec\alpha$, so (9) links *A* to cut obliquity. Real fibre cross-sections are polygonal rather than circular even in strictly transverse cuts, so the apparent obliquity $\alpha_{\text{app}} = \arccos(1/a)$ is an upper bound on the true cut angle.

Synthesis. Combining Propositions 2 and 3, the anisotropy of a transverse muscle section is the phasor sum of the contributions of fibre outlines, connective-tissue septa and fibre interiors, $Ae^{2i\psi} = \varepsilon_{\text{bnd}} A_{\text{bnd}} e^{2i\psi_{\text{bnd}}} + \varepsilon_{\text{sep}} A_{\text{sep}} e^{2i\psi_{\text{sep}}} + \varepsilon_{\text{int}} A_{\text{int}} e^{2i\psi_{\text{int}}}$. Proposition 3 predicts the first term from fibre shape and arrangement, Proposition 1 splits each term

into local order and alignment, and the observed A can be compared with each prediction. In a field without wide septa, $A \approx \varepsilon_{\mathrm{bnd}} R_P \bar{A}_{\mathrm{shape}}$; where septa are present, their term must be added (Figure 1c).

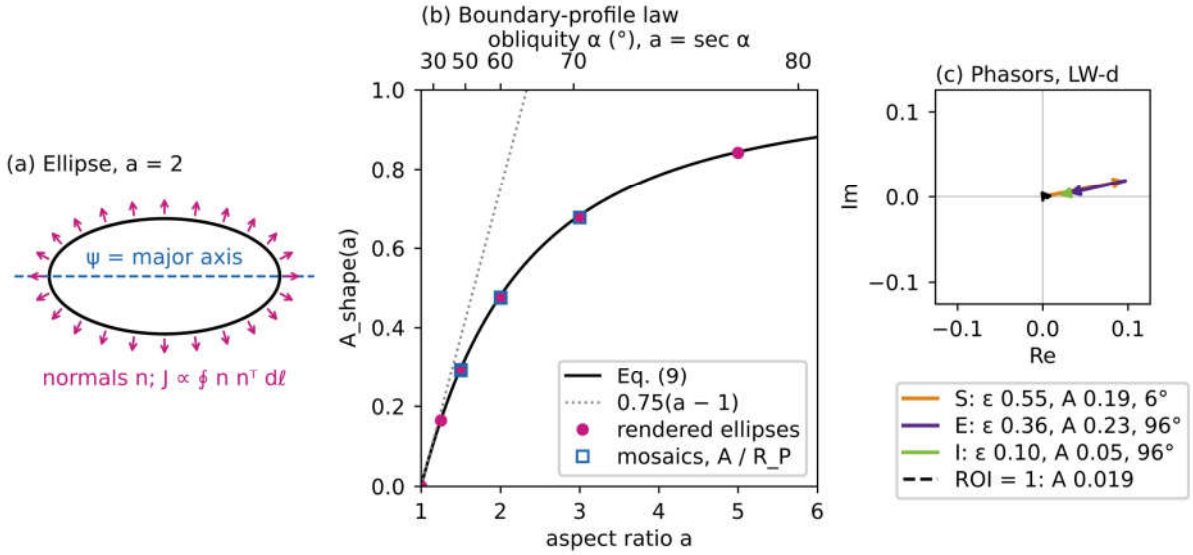


Figure 1. New theoretical results. (a) Boundary normals of an elliptical profile (aspect ratio a = 2); the structure matrix is proportional to $\oint \mathbf{n}\mathbf{n}^{\mathrm{T}}\mathrm{d}\ell$ and the texture axis is the major axis. (b) Boundary-profile law, Eq. (9) (solid line), its small-elongation approximation (dotted), anisotropy measured on rendered ellipses at s = 2 px (circles) and on mosaics of 60 ellipses divided by the resultant length R_P of their axes (squares); top axis: obliquity α of a circular cylinder with a = sec α. (c) Phasor diagram of Eq. (6) for the Large White detail field (LW-d): septal (S) and endomysial (E) contributions with nearly perpendicular axes cancel, and the ROI = 1 phasor (dashed) is short; I, fibre interior; legend entries give energy share ε, anisotropy A and axis ψ of each compartment.

References for isotropy and uncertainty. As in the earlier studies, an observed A is compared with the 95th percentile of A over 200 isotropic surrogates generated from the radially averaged Fourier amplitude of the same image with random phases (Theiler et al., 1992), which share the radial spectrum and therefore the finite-sample floor of A; uncertainty is estimated by a block bootstrap (Künsch, 1989), with 8 × 8 blocks for ROI = 1 and 6 × 6 blocks for each ROI of the four-ROI configuration, 1000 and 500 resamples respectively; the ROI is divided into a grid of 8 × 8 (or 6 × 6) blocks, which are resampled with replacement. The surrogate P-value is P = (1 + n≥)/(1 + N), where n≥ is the number of the N = 200 surrogates whose anisotropy is at least the observed one, so that the smallest attainable value is 1/201 = 0.005. The surrogates test departure from an isotropic Gaussian null model with the same radial spectrum, and the bootstrap describes spatial variability within a field, not variability between animals; tests repeated over panels, scales and ROIs are not corrected for multiplicity and are read descriptively. The scale-normalised energy $s^2\mathrm{tr}\mathbf{J}_s$, which equals the rate of variance loss per unit log-scale (Lindeberg, 1998), was evaluated at 15 log-spaced scales between 1 and 24 px, and its maximum s^* was refined by a parabola in log s.

Material and Method

Test images. Eight panels were taken from two open-access articles (Table 2, Figure 2). From Odung et al. (2025), wild boar (*Sus scrofa*) from Timor Island, three animals: transverse sections of *longissimus dorsi* (LD, Fig. 5A of the source; panel WB-LDt) and *biceps femoris* (BF, Fig. 5B; WB-BFt), a transverse LD section with intramuscular adipocytes (Fig. 3; WB-LDa) and a longitudinal LD section (Fig. 4A; WB-LDl), all H&E at 40×. From Wang et al. (2024), *longissimus dorsi* of male Xiang (XP) and Large White (LW) pigs aged 5.5 months (ten per breed in the source study), H&E transverse sections at two magnifications (Fig. 1A of the source): an overview with a 200 µm scale bar (XP-

o, LW-o) and a detail field with a 50 µm scale bar (XP-d, LW-d). The source study reports higher intramuscular fat in Xiang than in Large White pigs (5.65 ± 0.78 % versus 2.43 ± 0.66 %), higher fibre density, and fibre diameters of about 40 and 61 µm (read from its Fig. 1C).

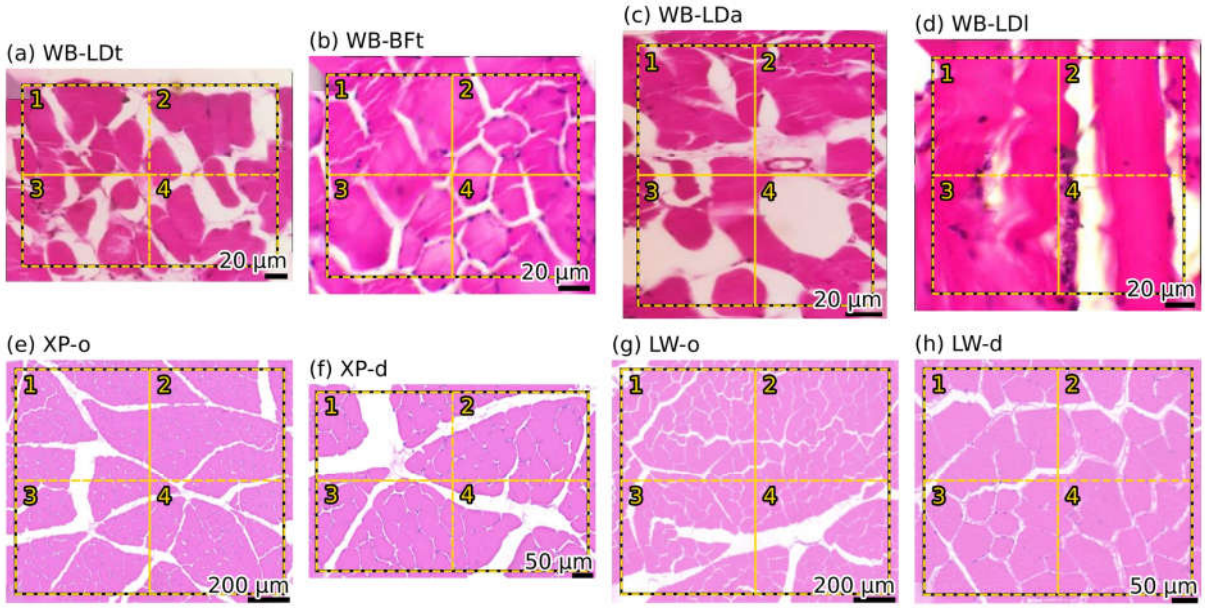


Figure 2. Test images after removal of annotations, with ROI = 1 (solid black) and the four ROIs of the R = 4 configuration (dashed, numbered 1–4). (a–d) Wild boar, H&E, 40×: (a) LD transverse, (b) BF transverse, (c) LD transverse with intramuscular adipocytes, (d) LD longitudinal; reproduced from Odung et al. (2025), Acta Veterinaria Indonesiana, CC BY-SA 4.0. (e–h) *Longissimus dorsi*, H&E, transverse: (e) Xiang pig, overview, (f) Xiang pig, detail, (g) Large White, overview, (h) Large White, detail; reproduced from Wang et al. (2024), Scientific Reports, CC BY 4.0. Scale bars redrawn from the calibration of each panel.

Image sources and permission to reproduce. Wang et al. (2024) is published in Scientific Reports under the Creative Commons Attribution 4.0 International licence (CC BY 4.0). The journal page of Odung et al. (2025) in Acta Veterinaria Indonesiana states the Creative Commons Attribution-ShareAlike 4.0 licence (CC BY-SA 4.0); the PDF carries only a copyright line. Both licences permit reuse and adaptation with attribution; CC BY-SA requires that adapted material be shared under the same licence, so Figures 2, 4, 6, 7 and 9, which contain adapted wild boar images, are distributed under CC BY-SA 4.0. The panels were extracted at their native resolution from the PDFs, cropped to single panels and processed as described below; all derived panels are new analyses by the author.

Preparation and calibration. Panel letters, arrows, hand-drawn outlines and scale bars were masked and filled by fast-marching inpainting (Telea, 2004); the inpainted share of each ROI is reported in Table 2 and was at most 8.2 %. The 50 µm and 200 µm bars of the Scientific Reports panels measure 45 and 72 px; the 30 µm bars of the wild boar panels measure 34–60 px because the source panels were resized differently. The dashed box drawn in Fig. 1A of Wang et al. (2024) to indicate the detail field is schematic: the bar ratio implies a magnification ratio of 2.5 between overview and detail. All lengths are given in µm from the bar calibration. Luminance was computed as $Y = 0.299R + 0.587G + 0.114B$ and z-scored per panel. Because the wild boar panels are small (257–289 px wide), ROI = 1 is the central region left after removing a 16-px margin (instead of the 48 px used for the human and fish images), which equals twice the largest derivative scale (only the aggregation is restricted to the ROI, the filters being applied to the whole panel); ROI = 4 is its partition into four equal quadrants (1 upper left, 2 upper right, 3 lower left, 4 lower right). Filters were applied to the whole panel with reflective boundaries and aggregated over each ROI.

Table 2

Test panels. Sources: [a] Odung et al. (2025); [b] Wang et al. (2024). LD, *longissimus dorsi*; BF, *biceps femoris*. ROI = 1 is the panel without a 16-px margin; luminance skewness and kurtosis over ROI = 1 (Gaussian: 0 and 3)

Panel	*Specimen and section*	*Source*	*Raster (px)*	*Scale bar*	*µm/px*	*ROI = 1 (µm)*	*Inpainted share of ROI*	*Skewness / kurtosis*
WB-LDt	Wild boar LD, transv., 40×	Fig. 5A [a]	287 × 213	30 µm = 34 px	0.882	225 × 160	7.8 %	0.68 / 1.82
WB-BFt	Wild boar BF, transv., 40×	Fig. 5B [a]	257 × 213	30 µm = 42 px	0.714	161 × 129	7.6 %	1.22 / 3.92
WB-LDa	Wild boar LD, transv., adipocytes, 40×	Fig. 3 [a]	289 × 316	30 µm = 60 px	0.500	128 × 142	4.0 %	0.41 / 1.41
WB-LDl	Wild boar LD, longit., 40×	Fig. 4A [a]	258 × 244	30 µm = 41 px	0.732	165 × 155	8.2 %	1.55 / 4.29
XP-o	Xiang LD, transv., overview	Fig. 1A [b]	492 × 417	200 µm = 72 px	2.778	1278 × 1069	0.5 %	1.68 / 4.41
XP-d	Xiang LD, transv., detail	Fig. 1A [b]	610 × 413	50 µm = 45 px	1.111	642 × 423	0.3 %	1.08 / 2.61
LW-o	Large White LD, transv., overview	Fig. 1A [b]	492 × 417	200 µm = 72 px	2.778	1278 × 1069	0.5 %	1.65 / 4.24
LW-d	Large White LD, transv., detail	Fig. 1A [b]	489 × 417	50 µm = 45 px	1.111	508 × 428	0.4 %	2.16 / 7.08

Compartments, segmentation and synthetic verification. For Proposition 2, each ROI was partitioned at s = 2 px into three compartments using an Otsu threshold (Otsu, 1979) of the smoothed luminance: fibre interior (fibre-coloured pixels eroded by 3 px), septal spaces (clear regions surviving a morphological opening with a disc of 5 µm radius, i.e. wider than about 10 µm, dilated by 3 px to include their borders) and the endomysial band (the rest of the interfibre band). For the WB-LDa panel, adipocytes were identified as clear, convex (solidity > 0.85), rounded (circularity ≥ 0.5) regions larger than 300 µm². For Proposition 3, fibre profiles were segmented by a white top-hat filter and Otsu threshold for the interfibre lines, h-maxima markers on the smoothed distance transform and watershed splitting (Vincent & Soille, 1991); profiles smaller than 150 µm² or touching the panel border were discarded, and the area, perimeter, equivalent diameter, major and minor axes, orientation and circularity ($4\pi \cdot \text{area}/\text{perimeter}^2$) of each profile were computed from its second moments. Proposition 3 was verified on rendered ellipses (aspect ratios 1–5, 4× supersampling) and on mosaics of 60 non-overlapping ellipses with axes drawn from a uniform or von Mises distribution, and Proposition 1 was checked with periodic filtering on each whole panel. All computations used the reference implementation of the tensor (Python, NumPy, SciPy, OpenCV, scikit-image) without changes to its definitions.

Results

Verification of the new results. Table 3 compares Eq. (9) with rendered ellipses and Eq. (10) with synthetic mosaics. For single ellipses the measured A at s = 2 px differs from the closed form by at most 0.003 (at most 0.006 at s = 4 px), and the texture axis coincides with the major axis. For mosaics with uniformly or partially aligned axes, the prediction of Eq. (10) differs from the measured A by at most 0.004 and the axis by at most 0.5°. The uniform mosaic illustrates the role of alignment: its profiles have A_{shape} = 0.296 each, but their axes nearly cancel and the mosaic has A = 0.044. With periodic filtering over whole panels, A_ρ was constant over ρ = 0–64 px to a relative deviation of 1e-15, and $\bar{\kappa}_E$ and R were monotone in every panel, as Proposition 1 requires.

Table 3

Synthetic verification of the boundary-profile law. Theory: Eq. (9) for single ellipses and Eq. (10) for mosaics; R_P, perimeter-weighted resultant length of the profile axes. Axis error: difference between measured texture axis and major axis (single ellipse) or predicted axis (mosaic); n/a, the axis of a circle is undefined

Test	*Aspect a*	*Axis concentration*	*Theory*	*Measured A (s = 2 px)*	*Axis error (°)*
Single ellipse	1.00	–	0.000	0.000	n/a
Single ellipse	1.25	–	0.166	0.165	0.02
Single ellipse	1.50	–	0.296	0.294	0.01
Single ellipse	2.00	–	0.480	0.477	0.00
Single ellipse	3.00	–	0.682	0.679	0.00
Single ellipse	5.00	–	0.844	0.842	0.00
Mosaic, 60 ellipses	1.50	uniform (R_P = 0.15)	0.044	0.044	0.5
Mosaic, 60 ellipses	1.50	von Mises κ = 2 (R_P = 0.74)	0.218	0.216	0.1
Mosaic, 60 ellipses	2.00	von Mises κ = 2 (R_P = 0.60)	0.287	0.284	0.1
Mosaic, 60 ellipses	2.00	von Mises κ = 8 (R_P = 0.93)	0.444	0.441	0.0
Mosaic, 60 ellipses	3.00	von Mises κ = 4 (R_P = 0.86)	0.587	0.583	0.1

Single-ROI tensor: anisotropy and axis. Table 4 gives the $R = 1$ tensor at $s = 2$ px and Figure 3 the anisotropy and axis at the four scales, in μm.

Table 4

$R = 1$ tensor at $s = 2$ px: share of D_2 energy at the four configured orientations, anisotropy index A with 95 % bootstrap CI, 95th percentile of A for isotropic surrogates, and texture axis ψ (°, from $+x$, y upward) with 95 % CI

Panel	*θ = 0*	*θ = π/4*	*θ = π/2*	*θ = 3π/4*	*A [95 % CI]*	*Null 95th pct*	*ψ (°) [95 % CI]*
WB-LDt	0.272	0.284	0.228	0.216	0.161 [0.053, 0.311]	0.047	118.3 [96.0, 139.1]
WB-BFt	0.279	0.266	0.221	0.234	0.133 [0.049, 0.285]	0.033	104.0 [71.6, 122.6]
WB-LDa	0.215	0.286	0.285	0.214	0.201 [0.112, 0.326]	0.033	157.4 [141.2, 171.6]
WB-LDl	0.424	0.255	0.076	0.245	0.697 [0.613, 0.760]	0.054	90.8 [87.5, 94.2]
XP-o	0.199	0.251	0.301	0.249	0.206 [0.101, 0.330]	0.012	179.4 [160.3, 200.5]
XP-d	0.232	0.205	0.268	0.295	0.195 [0.110, 0.313]	0.011	33.9 [12.7, 51.3]
LW-o	0.211	0.197	0.289	0.303	0.262 [0.180, 0.349]	0.012	26.8 [15.3, 39.0]
LW-d	0.245	0.250	0.255	0.250	0.019 [0.013, 0.168]	0.012	2.6 [-80.9, 84.3]

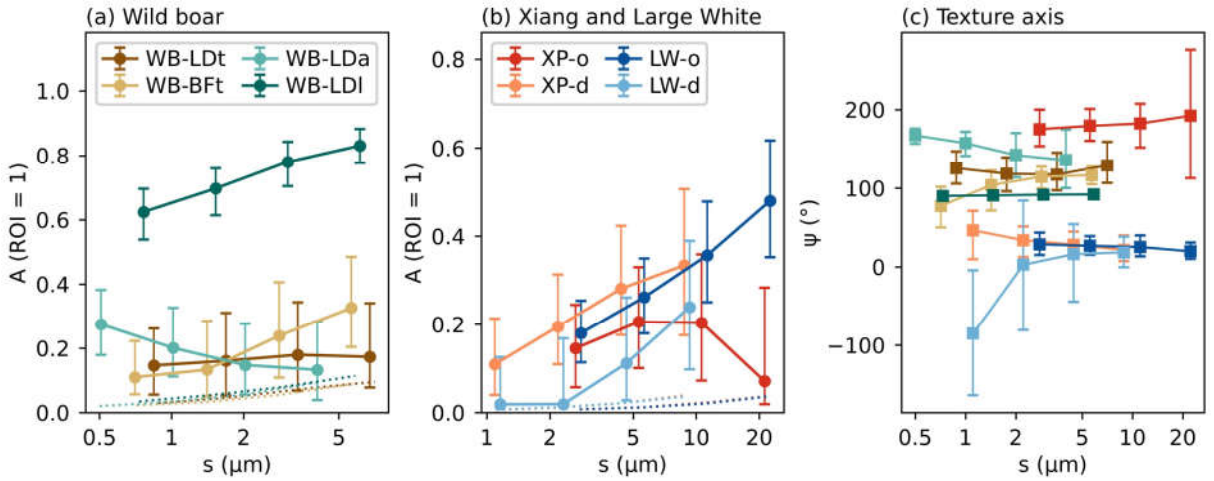


Figure 3. Single-ROI tensor against physical scale. (a) Wild boar and (b) domestic pig panels: anisotropy index A with 95 % bootstrap CI at $s = 1, 2, 4, 8$ px converted to μm; dotted lines: 95th percentile of isotropic surrogates. (c) Texture axis ψ with 95 % CI (unwrapped about its value at $s = 2$ px).

Interpretation. All eight panels exceed the isotropic floor at every scale ($P \leq 0.005$ at s = 1–4 px in all panels; $P \leq 0.01$ at s = 8 px), but the anisotropy is low in transverse sections and high in the longitudinal one. At s = 2 px, A of the transverse panels ranges from 0.019 (LW-d) to 0.262 (LW-o), whereas the longitudinal wild boar section has A = 0.697 (0.613–0.760) with an axis of 90.8° (87.5–94.2°), i.e. along the vertically running fibres; its A increases with scale to 0.831 at s = 8 px, as for oriented stripes, whose contrast is preserved by coarse operators along the stripes. The wild boar transverse panels give A = 0.161 (LD) and 0.133 (BF), with wide intervals because the panels are small (blocks of about 30 px). LW-d is the only panel whose A at s = 1–2 px is close to the floor (0.019 against 0.012; P = 0.005): at the fibre scale the Large White detail field is almost isotropic, and its axis is undetermined (CI -80.9–84.3°). Reading A as the contrast (max − min)/(max + min) of the four sampled energies underestimates it, because the true extremes need not fall on the sampled orientations (for example, 0.134 against 0.161 for WB-LDt; the full index computed from the structure matrix is exact).

The scale dependence separates the two breeds (Figure 3b, Table 5). In the overviews, A of Large White increases monotonically with scale, from 0.180 at s = 1 px (2.8 µm) to 0.480 at s = 8 px (22 µm), with a stable axis (28.5° → 19.7°), whereas A of Xiang rises to 0.206 at s = 2 px and falls to 0.071 at s = 8 px. At s = 8 px the intervals do not overlap (Large White 0.352–0.617, Xiang 0.019–0.284). At fascicle scale the Large White section is therefore organised along one dominant direction, whereas the Xiang section is not; Figure 2 shows why: the perimysial septa of LW-o run mainly in one direction, those of XP-o branch in several. In the detail fields the order is reversed at fine scale (XP-d 0.195, LW-d 0.019 at s = 2 px), but the intervals overlap.

Table 5

Scale dependence at R = 1: anisotropy index A (95th percentile of isotropic surrogates in parentheses) at the four configured scales, drift of the texture axis between s = 1 and 8 px, characteristic scale s^* of the scale-normalised energy and its half-maximum band, in µm

Panel	*µm/px*	*A (null), s = 1 px*	*s = 2 px*	*s = 4 px*	*s = 8 px*	*ψ (°), s = 1 → 8 px*	*s* (µm)*	*Half-max. band (µm)*
WB-LDt	0.88	0.146 (0.029)	0.161 (0.047)	0.179 (0.073)	0.173 (0.095)	125 → 129	5.9	1.7–16.9
WB-BFt	0.71	0.110 (0.023)	0.133 (0.033)	0.239 (0.055)	0.326 (0.089)	77 → 116	2.1	0.7–5.5
WB-LDa	0.50	0.274 (0.020)	0.201 (0.033)	0.148 (0.055)	0.133 (0.093)	167 → 136	5.0	1.6–12.0
WB-LDl	0.73	0.624 (0.035)	0.697 (0.054)	0.780 (0.080)	0.831 (0.114)	90 → 92	6.3	2.3–14.0
XP-o	2.78	0.145 (0.007)	0.206 (0.012)	0.204 (0.022)	0.071 (0.037)	175 → 12	13.5	2.8–53.1
XP-d	1.11	0.109 (0.006)	0.195 (0.011)	0.281 (0.022)	0.334 (0.039)	46 → 22	13.6	1.7–26.7
LW-o	2.78	0.180 (0.007)	0.262 (0.012)	0.357 (0.020)	0.480 (0.036)	29 → 20	15.9	3.5–66.7
LW-d	1.11	0.019 (0.007)	0.019 (0.012)	0.111 (0.022)	0.239 (0.036)	95 → 18	5.2	1.1–16.9

Four-ROI tensor: regional heterogeneity. Table 6 and Figure 4 report the R = 4 tensor at s = 2 px, and Table 7 the comparison with R = 1.

Table 6

$R = 4$ tensor at $s = 2$ px: D_2 shares, anisotropy index A with 95 % bootstrap CI, 95th percentile of A for isotropic surrogates of the same ROI, and texture axis ψ (°) with 95 % CI. ROI numbers as in Figure 2. †, A not above the isotropic floor

ROI	θ = 0	θ = π/4	θ = π/2	θ = 3π/4	A [95 % CI]	Null 95th pct	ψ (°) [95 % CI]
WB-LDt-1	0.308	0.281	0.192	0.219	0.265 [0.154, 0.468]	0.140	104.0 [77.4, 119.4]
WB-LDt-2	0.251	0.302	0.249	0.198	0.209 [0.097, 0.397]	0.145	134.6 [108.1, 164.9]
WB-LDt-3 †	0.283	0.246	0.217	0.254	0.133 [0.053, 0.310]	0.149	86.3 [46.0, 131.0]
WB-LDt-4	0.250	0.305	0.250	0.195	0.221 [0.099, 0.449]	0.137	135.2 [119.1, 178.8]
WB-BFt-1	0.298	0.292	0.202	0.208	0.254 [0.052, 0.524]	0.127	110.7 [77.8, 156.8]
WB-BFt-2 †	0.272	0.237	0.228	0.263	0.103 [0.040, 0.330]	0.121	74.2 [18.8, 119.2]
WB-BFt-3	0.277	0.268	0.223	0.232	0.131 [0.042, 0.427]	0.116	106.9 [30.9, 174.0]
WB-BFt-4	0.276	0.272	0.224	0.228	0.139 [0.039, 0.381]	0.124	110.1 [34.4, 159.0]
WB-LDa-1	0.216	0.323	0.284	0.177	0.321 [0.169, 0.504]	0.129	147.5 [133.6, 164.7]
WB-LDa-2	0.189	0.236	0.311	0.264	0.251 [0.044, 0.465]	0.115	6.7 [-9.0, 66.5]
WB-LDa-3 †	0.242	0.257	0.258	0.243	0.044 [0.022, 0.316]	0.113	159.5 [84.4, 243.2]
WB-LDa-4	0.209	0.329	0.291	0.171	0.356 [0.125, 0.550]	0.115	148.8 [130.3, 167.0]
WB-LDl-1	0.325	0.198	0.175	0.302	0.364 [0.181, 0.516]	0.161	72.6 [49.5, 96.3]
WB-LDl-2	0.440	0.251	0.060	0.249	0.758 [0.656, 0.846]	0.151	90.1 [84.0, 96.9]
WB-LDl-3	0.347	0.265	0.153	0.235	0.394 [0.157, 0.584]	0.155	94.2 [76.6, 106.2]
WB-LDl-4	0.457	0.273	0.043	0.227	0.833 [0.791, 0.880]	0.150	93.1 [89.5, 95.9]
XP-o-1	0.196	0.304	0.304	0.196	0.306 [0.104, 0.534]	0.057	157.7 [131.9, 173.3]
XP-o-2	0.216	0.280	0.284	0.220	0.180 [0.056, 0.416]	0.062	159.3 [120.2, 213.9]
XP-o-3	0.202	0.163	0.298	0.337	0.397 [0.241, 0.563]	0.060	30.6 [15.2, 44.5]
XP-o-4	0.184	0.276	0.316	0.224	0.283 [0.140, 0.443]	0.054	169.3 [151.9, 192.2]
XP-d-1	0.224	0.228	0.276	0.272	0.135 [0.032, 0.350]	0.056	20.3 [-33.8, 98.2]
XP-d-2	0.232	0.152	0.268	0.348	0.398 [0.315, 0.542]	0.054	39.8 [21.7, 58.6]
XP-d-3	0.256	0.206	0.244	0.294	0.177 [0.051, 0.429]	0.053	49.1 [-12.1, 66.2]
XP-d-4	0.218	0.233	0.282	0.267	0.147 [0.057, 0.324]	0.049	14.2 [-17.3, 54.0]
LW-o-1	0.226	0.178	0.274	0.322	0.304 [0.202, 0.438]	0.063	35.8 [20.1, 47.8]
LW-o-2	0.237	0.200	0.263	0.300	0.207 [0.105, 0.338]	0.057	37.7 [14.8, 56.0]
LW-o-3	0.199	0.216	0.301	0.284	0.247 [0.114, 0.406]	0.057	17.0 [-0.6, 47.6]
LW-o-4	0.193	0.197	0.307	0.303	0.311 [0.165, 0.511]	0.060	21.3 [3.1, 45.3]
LW-d-1	0.200	0.206	0.300	0.294	0.268 [0.122, 0.426]	0.057	20.7 [-0.3, 44.9]
LW-d-2	0.240	0.265	0.260	0.235	0.071 [0.025, 0.267]	0.059	152.5 [81.1, 222.6]
LW-d-3	0.264	0.280	0.236	0.220	0.131 [0.027, 0.368]	0.058	122.4 [59.8, 188.6]
LW-d-4	0.297	0.241	0.203	0.259	0.193 [0.084, 0.318]	0.060	84.6 [63.4, 112.6]

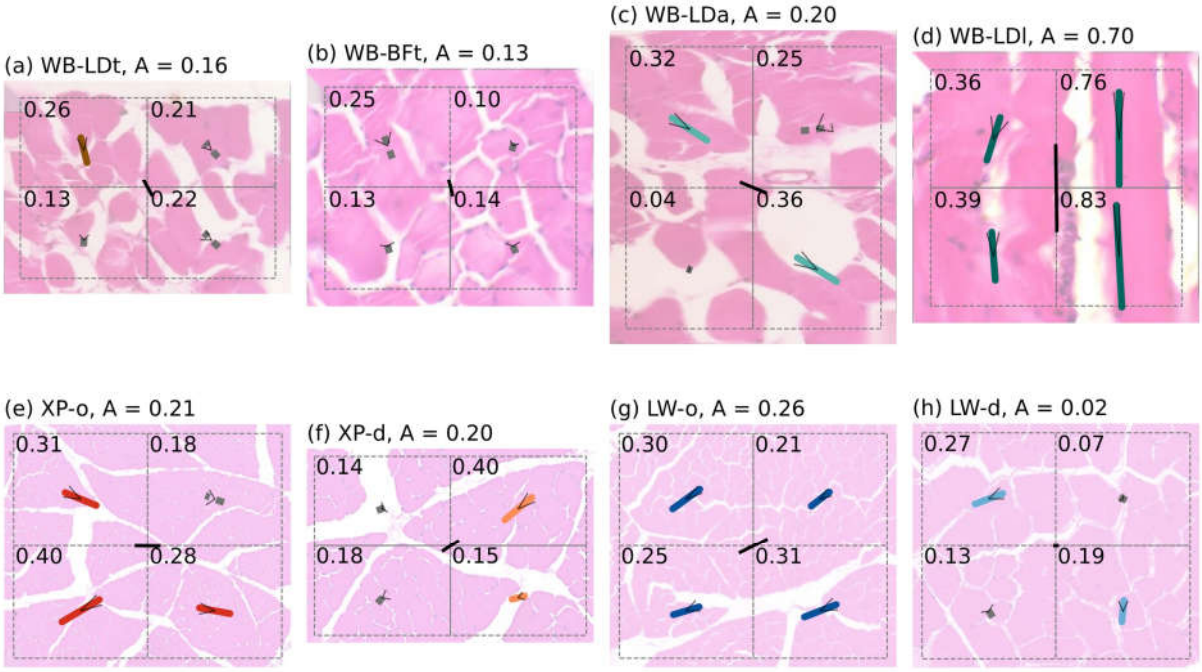


Figure 4. Four-ROI tensor shown as orientation glyphs on each panel (s = 2 px); the number in each ROI is its A, and the panel title gives A of ROI = 1. Bar orientation, texture axis ψ of the ROI; bar length proportional to A; thin black lines, 95 % CI of the axis; coloured solid bars, lower CI limit of A above the isotropic floor; grey dotted bars, not resolved from the floor. Central black bar: ROI = 1.

Interpretation. Of the 32 ROIs, 29 have A above their isotropic floor and 18 have the lower confidence limit above it; the three exceptions (WB-LDt3, WB-BFt2, WB-LDa3) are wild boar quadrants of only 90–142 px per side, where the floor is high (0.11–0.15). Regional heterogeneity follows the pattern predicted by the pooling inequality. Where the quadrant axes agree, R = 1 loses little relative to the energy-weighted mean of the quadrants (LW-o, circular SD of axes 9.0°, loss 5 %; WB-LDl, 8.8°, loss 1 %); where they disagree the loss is large (XP-o, 21.8°, 31 %; WB-LDt, 21.7°, 22 %), and in LW-d, whose quadrant axes are spread by 49.9°, the four quadrants have A = 0.07–0.27 but the whole field has A = 0.019, a loss of 88 %. The near-isotropy of LW-d at the fibre scale is therefore not an absence of local organisation but a cancellation between regions with different axes.

Table 7

Regional pooling (Proposition 2a, equal areas) and coherence–alignment readings (Proposition 1) at s = 2 px. Loss = 1 − A/(energy-weighted mean). ρ_c, integration scale at which $\bar{\kappa}_E = R$; Eq. (5) predicts $\bar{\kappa}_E(\rho_c) = R(\rho_c) = \sqrt{A}$.

Panel	*A (ROI = 1)*	*Energy-weighted mean of 4 ROIs, Eq. (6)*	*Loss (%)*	*Circular SD of ROI axes (°)*	*ρc (μm)*	*√A*	*Mean local coherence κ (ρ = 10 px)*
WB-LDt	0.161	0.206	22	21.7	11.8	0.401	0.47
WB-BFt	0.133	0.149	11	15.3	9.8	0.365	0.46
WB-LDa	0.201	0.239	16	15.9	7.1	0.448	0.57
WB-LDl	0.697	0.707	1	8.8	2.9	0.835	0.64
XP-o	0.206	0.300	31	21.8	86.7	0.453	0.60
XP-d	0.195	0.216	10	14.4	42.3	0.442	0.56
LW-o	0.262	0.274	5	9.0	46.5	0.511	0.53
LW-d	0.019	0.160	88	49.9	68.1	0.138	0.49

Local coherence and alignment. Figure 5 shows $\bar{\kappa}_E(\rho)$, $R(\rho)$ and their product for every panel. In all panels $\bar{\kappa}_E$ decreases and R increases with ρ, and their product stays close to A: on the ROI with reflective boundaries, A_ρ deviates from A by at most 7 % for $\rho \leq \rho_c$ in seven panels. The exception is LW-d (deviation 104 %, from 0.019 to 0.039), where A is so small that the boundary leakage of the window is comparable with it.

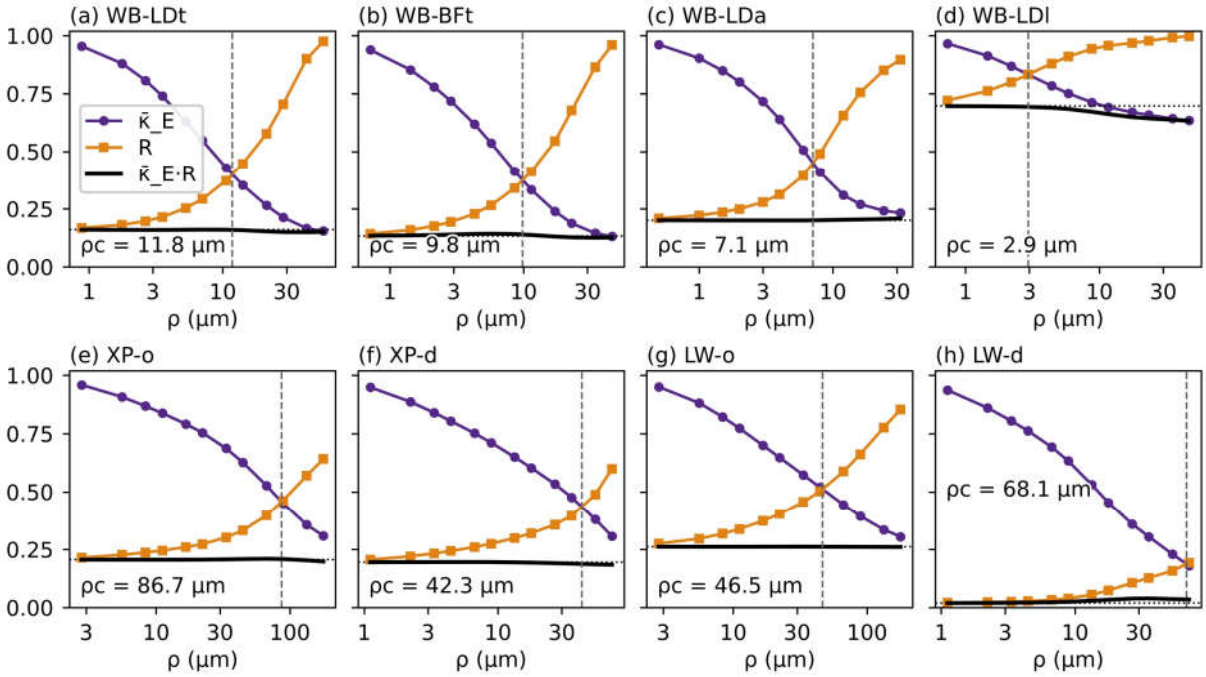


Figure 5. Coherence–alignment factorisation (Proposition 1) at s = 2 px. Energy-weighted local coherence $\bar{\kappa}_E$ (circles), resultant length of local axes R (squares) and their product A_ρ (thick line) against the integration scale ρ in µm; dotted line, A of ROI = 1; dashed line, crossover scale ρ_c (value given in each panel).

Interpretation. The crossover scale ρ_c separates the panels by the size of their orientation domains. In the wild boar transverse sections ρ_c = 7.1–11.8 µm, about one quarter to two fifths of the median fibre diameter (27–31 µm): orientation is consistent within one fibre outline and changes from fibre to fibre. In the domestic pig sections ρ_c is 42–87 µm, of the order of one or more fibre diameters, because there the dominant edges are long septa: ρ_c is largest in XP-o (86.7 µm), whose septa change direction between fascicles. In the longitudinal section ρ_c is only 2.9 µm, because the alignment R is already high at small windows: the fibres share one axis across the whole field, so local and global orientation agree. Two sections with similar A can thus differ in structure: WB-LDt and XP-d have A = 0.161 and 0.195, but ρ_c = 11.8 and 42.3 µm.

Tissue compartments. Table 8 and Figure 6 decompose A over septal spaces, endomysial band and fibre interior (Proposition 2).

Table 8

Compartment decomposition at s = 2 px, Eq. (6): area share p, energy share ε, anisotropy A and axis ψ (°) of each compartment. $\Sigma\ \varepsilon_c A_c$ is the upper bound of Proposition 2a; loss = $1 - A/\Sigma\ \varepsilon_c A_c$. The reconstruction of A from the compartment phasors was exact in all panels, as Eq. (6) is an identity for any partition; the assignment of pixels to septa, endomysium and fibre interior depends on the segmentation thresholds

Panel	*Septal: p / ε / A / ψ*	*Endomysial: p / ε / A / ψ*	*Interior: p / ε / A / ψ*	*Σ ε_c A_c*	*A (ROI = 1)*	*Loss (%)*
WB-LDt	0.34 / 0.59 / 0.197 / 117.0	0.15 / 0.33 / 0.107 / 118.2	0.51 / 0.08 / 0.134 / 133.3	0.162	0.161	1
WB-BFt	0.01 / 0.00 / 0.203 / 170.7	0.36 / 0.89 / 0.160 / 105.5	0.62 / 0.11 / 0.104 / 37.9	0.154	0.133	13
WB-LDa	0.35 / 0.47 / 0.127 / 133.4	0.14 / 0.42 / 0.337 / 164.2	0.50 / 0.11 / 0.234 / 170.3	0.227	0.201	12
WB-LDl	0.18 / 0.62 / 0.791 / 91.0	0.06 / 0.21 / 0.661 / 90.7	0.76 / 0.17 / 0.398 / 89.0	0.697	0.697	0
XP-o	0.22 / 0.86 / 0.225 / 179.5	0.04 / 0.07 / 0.162 / 3.4	0.75 / 0.07 / 0.039 / 146.5	0.207	0.206	1
XP-d	0.25 / 0.69 / 0.271 / 28.9	0.06 / 0.21 / 0.122 / 66.2	0.68 / 0.10 / 0.092 / 81.9	0.222	0.195	12
LW-o	0.21 / 0.72 / 0.349 / 23.7	0.07 / 0.13 / 0.070 / 45.1	0.72 / 0.15 / 0.148 / 67.3	0.284	0.262	8
LW-d	0.12 / 0.55 / 0.191 / 5.7	0.13 / 0.36 / 0.227 / 96.4	0.75 / 0.10 / 0.053 / 95.6	0.191	0.019	90

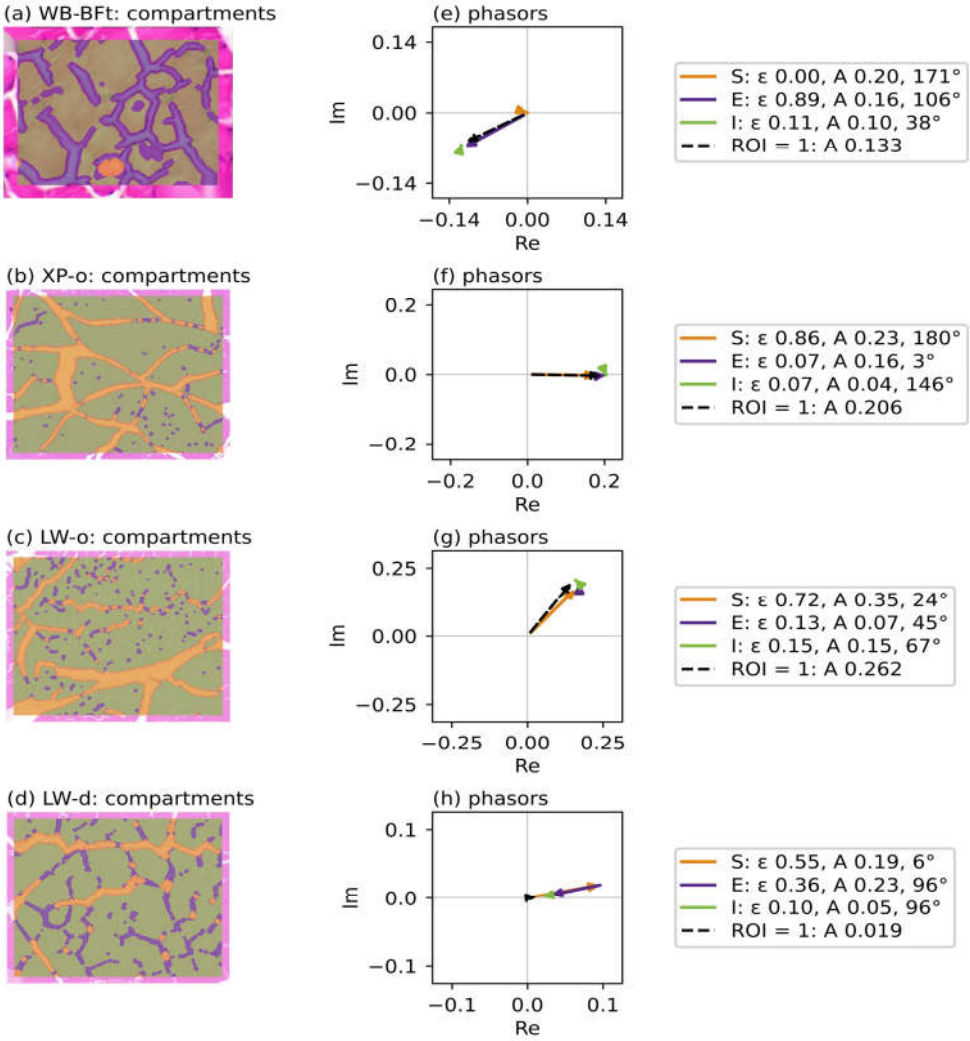


Figure 6. Tissue compartments and their phasors. (a–d) Septal spaces (orange), endomysial band (purple) and fibre interior (green) within ROI = 1 for WB-BFt, XP-o, LW-o and LW-d. (e–h) Phasor diagrams of Eq. (6): each arrow is $\varepsilon_c A_c e^{2i\psi c}$; the dashed arrow is the ROI = 1 phasor $Ae^{2i\psi}$. Legends: S, septal; E, endomysial; I, fibre interior; energy share ε, anisotropy A and axis ψ of each compartment.

Interpretation. In every panel the interfibre band (septal plus endomysial compartments) carries most of the gradient energy (0.83–0.93) on a minority of the area (0.24–0.50), so *A* is a property of the connective-tissue boundaries rather than of the fibre interiors, whose energy share is 0.07–0.17. Which part of the band dominates depends on the field. In the overviews the septa carry most of the energy (XP-o ε = 0.86, LW-o 0.72) and fix the axis of the section (XP-o septa 179.5°, section 179.4°; LW-o 23.7° and 26.8°), with little loss (1 % and 8 %). In WB-BFt there are no wide septa (ε = 0.00) and the endomysial band alone determines *A*. The most instructive case is LW-d: septa (ε = 0.55, *A* = 0.191, ψ = 5.7°) and endomysium (ε = 0.36, *A* = 0.227, ψ = 96.4°) are both clearly oriented, but their axes differ by 91°, and by Eq. (7) they cancel: the upper bound is 0.191 and the observed *A* is 0.019, a loss of 90 %. In this field the interfibre lines that run between fibres are mostly perpendicular to the septum that crosses it, a configuration that a single anisotropy value cannot reveal.

Fibre-profile geometry and morphometry. Table 9 and Figure 7 give the morphometry of the segmented fibres and compare the anisotropy predicted from their shapes by Eq. (10) with that measured on the interfibre band.

Table 9

Morphometry of segmented fibre profiles within ROI = 1 (medians) and test of the boundary-profile law. R_P, perimeter-weighted resultant length of profile axes; mean A_{shape} from Eq. (9); *A* predicted from Eq. (10) with its axis ψ_{bnd}; measured *A*, axis and energy share ε of the interfibre band at *s* = 2 px. The longitudinal panel (2 complete profiles) is omitted

Panel	*Fibres*	*Eq. diameter (µm)*	*Minor axis (µm)*	*Aspect a*	*Circularity*	*R_P*	*Mean A_shape*	*A predicted [ψ]*	*Band A measured [ψ]*	*Band ε*
WB-LDt	18	29.9	25.6	1.49	0.61	0.41	0.337	0.137 [127.1]	0.165 [117.4]	0.92
WB-BFt	12	30.5	26.0	1.59	0.47	0.54	0.380	0.205 [103.9]	0.158 [105.6]	0.89
WB-LDa	10	26.6	22.9	1.59	0.55	0.69	0.356	0.245 [166.4]	0.200 [155.7]	0.89
XP-o	244	65.3	53.5	1.41	0.72	0.25	0.307	0.076 [113.4]	0.220 [179.8]	0.93
XP-d	76	52.3	42.4	1.46	0.68	0.26	0.304	0.079 [87.9]	0.216 [32.6]	0.91
LW-o	205	73.4	61.6	1.42	0.70	0.09	0.318	0.030 [69.8]	0.301 [24.5]	0.86
LW-d	43	66.7	53.3	1.47	0.62	0.13	0.308	0.041 [147.2]	0.026 [4.0]	0.91

Interpretation. The calibration is broadly consistent with the morphometry of the source study, although the agreement depends on the field. Wang et al. (2024) report fibre diameters of about 40 µm (Xiang) and 61 µm (Large White); the median minor-axis lengths of the segmented profiles are 42.4 µm in XP-d and 61.6 µm in LW-o (overview values: Xiang 53.5 µm, Large White 61.6 µm; detail: 42.4 and 53.3 µm), and the Large White/Xiang ratio in the detail fields is 1.26. Equivalent diameters are larger (52.3 and 66.7 µm in the detail fields) because they include the long axis. Wild boar fibres are smaller (median equivalent diameter 27–31 µm, minor axis 23–26 µm), consistent with the smaller fibres of wild pigs reported by Ruusunen & Puolanne (2004), although magnification and processing differ between the sources. The rounder, "oval" Xiang fibres and the "irregularly square" Large White fibres described by Wang et al. (2024) appear as a higher median circularity (XP-d 0.68, LW-d 0.62) at practically the same median aspect ratio (1.46 and 1.47): the difference is in the corners of the profiles, not in their elongation, and therefore does not change A_{shape} (0.30–0.32 in all domestic panels).

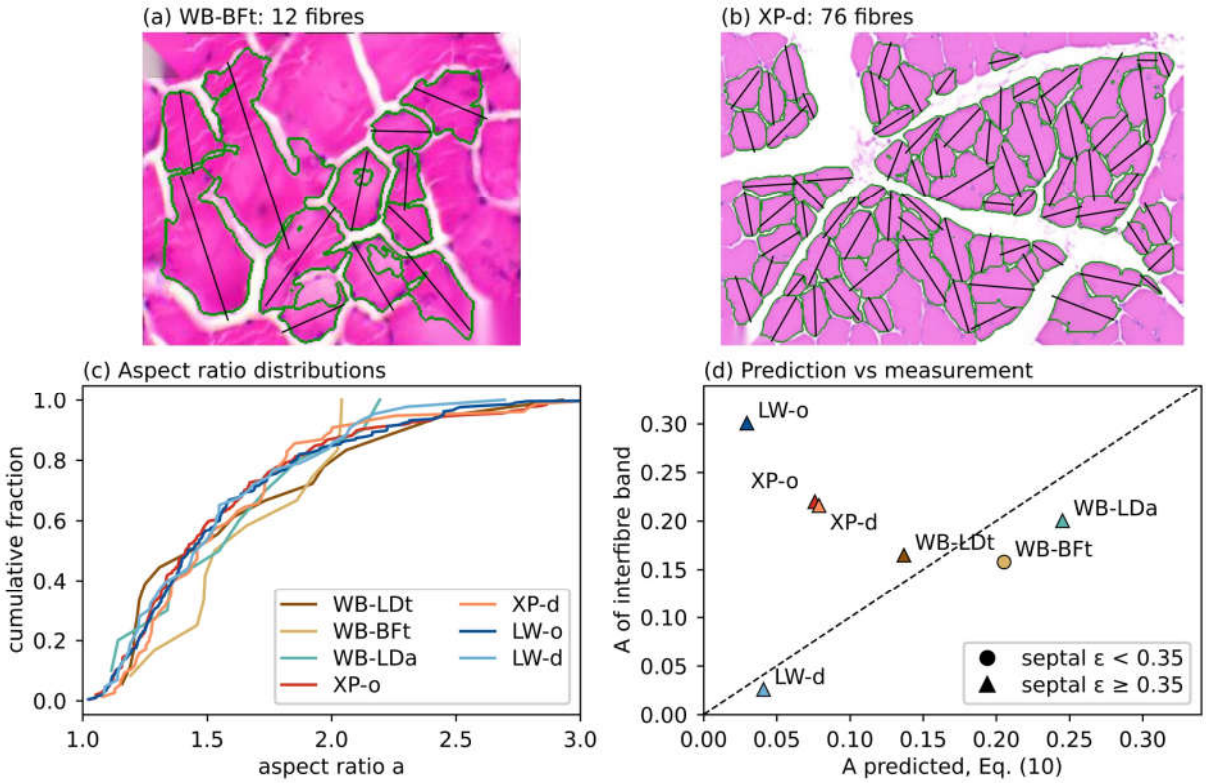


Figure 7. Fibre-profile geometry. (a,b) Segmented fibre profiles (green) with their major axes (black) for WB-BFt and XP-d. (c) Cumulative distributions of profile aspect ratio. (d) Anisotropy predicted from the fibre profiles by Eq. (10) against the anisotropy of the interfibre band; circles, panels in which septa carry less than 35 % of the energy; triangles, 35 % or more; letters as in Figure 2.

The boundary-profile law explains the band anisotropy where the band consists of closed fibre outlines. In WB-BFt (no septa) the prediction is 0.205 at 103.9° and the measurement 0.158 at 105.6°, an axis difference of 1.7°; in WB-LDt and WB-LDa the predictions 0.137 and 0.245 compare with measured 0.165 and 0.200, with axis differences of 10–11°, and in LW-d the prediction (0.041) and the measurement (0.026) are both close to zero. In these fields A is accounted for by the elongation of the fibre profiles (A_{shape} 0.31–0.38, apparent obliquity 47–51°) multiplied by their moderate alignment (R_P = 0.13–0.69). In the fields where septa carry most of the energy (XP-o, XP-d, LW-o) the band anisotropy (0.22–0.30) is about three to ten times the fibre-profile prediction (0.03–0.08) and its axis follows the septa, not the fibres. The fibres of these domestic pig sections are elongated (median a = 1.41–1.47) but not aligned (R_P = 0.09–0.26), so their outlines contribute little net anisotropy; the directional organisation of the section is carried by the perimysium.

Characteristic scale. Figure 8 shows the scale-normalised energy against scale in µm. In Xiang muscle the characteristic scale is the same at both magnifications (s^* = 13.5 µm in the overview and 13.6 µm in the detail field), as expected if s^* is a property of the tissue: the two rasters differ by a factor of 2.5 in pixel size. In Large White muscle the two values differ (15.9 and 5.2 µm): the overview contains wide septa, whose edges dominate the variance loss, whereas the detail field is dominated by the fine endomysial lines (Table 8). For wild boar, s^* is 5.0–6.3 µm in the LD panels and 2.1 µm in BF, whose interfibre spaces are the narrowest. As in human muscle, s* is read as the width of the dominant intensity transitions, about half of the width of the dominant interfibre spaces, not as a fibre size.

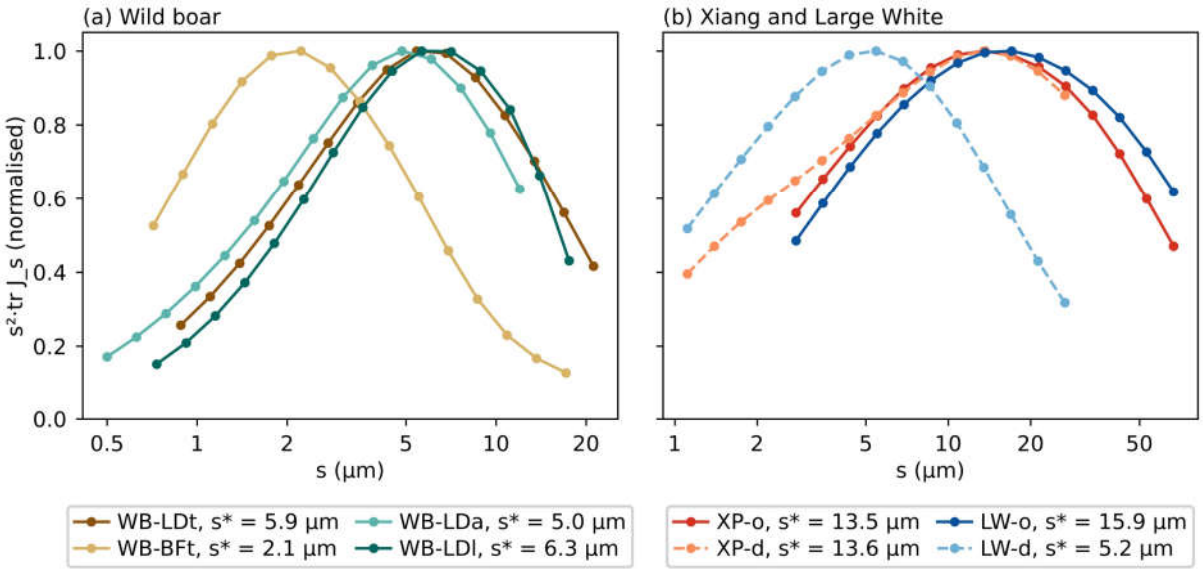


Figure 8. Scale-normalised derivative energy $s^2\mathrm{tr}\mathbf{J}_s$ (normalised to its maximum) against scale in µm for ROI = 1. (a) Wild boar; (b) Xiang and Large White at two magnifications (solid, overview; dashed, detail). The characteristic scale *s** is given in the legend.

Intramuscular adipocytes. In WB-LDa, 2 adipocytes (equivalent diameters 48, 24 µm) were detected; they cover 13 % of ROI = 1 and carry an energy share of 0.13 (Figure 9). Their compartment is not isotropic (*A* = 0.238, ψ = 141.5°; muscle 0.202, 160.2°), because two cells, one of them only partly inside the ROI, cannot average their boundary orientations; Eq. (6) still reconstructs *A* exactly, but the dilution law (8), which requires an isotropic compartment, does not apply. Regionally, the quadrant with 51 % adipocyte area (ROI 4) has the highest *A* (0.356; Table 6), whereas the quadrant without adipocytes but with irregular small fibres (ROI 3) is the only one at the isotropic floor. The adipocyte compartment, which includes the cell rims, has the same mean energy per pixel as the surrounding muscle (ratio 1.00), so its energy share equals its area share; this energy sits on the rims, and two rims cannot average out their orientation, so a few large adipocytes do not dilute *A*; a dilution effect of intramuscular fat is expected only for many small adipocytes, which these images do not contain.

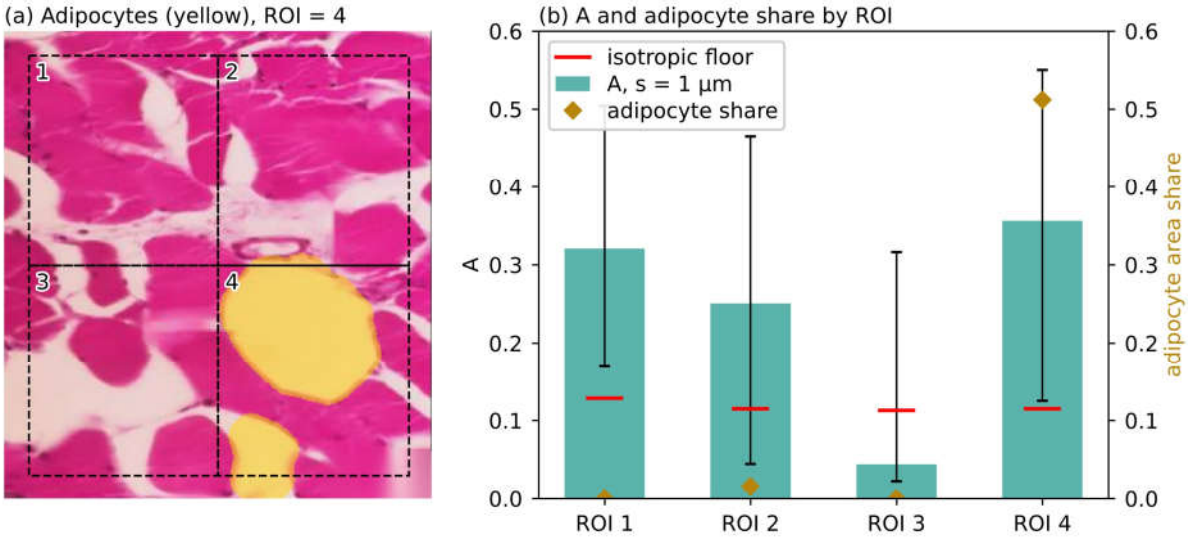


Figure 9. Intramuscular adipocytes in the wild boar LD section (WB-LDa). (a) Detected adipocytes (yellow) and the four ROIs. (b) Anisotropy index *A* of each ROI at *s* = 2 px (1 µm) with 95 % CI, isotropic floor (red), and adipocyte area share (diamonds, right axis).

Channels and distance between ROI tensors. Table 10 gives the channel means and directional modulation at s = 2 px, and Figure 10 the rank correlations of the channels over the 512 entries of the eight R = 4 tensors and a principal-component projection of the 32 ROI tensors.

Table 10

Channel means over θ and, in parentheses, directional modulation index (max − min)/(max + min) over the four orientations at s = 2 px (R = 1)

Channel	*WB-LDt*	*WB-BFt*	*WB-LDa*	*WB-LDl*	*XP-o*	*XP-d*	*LW-o*	*LW-d*
D1	0.0711	0.0976	0.0545	0.0528	0.063	0.0503	0.0677	0.0679
	(0.08)	(0.06)	(0.11)	(0.40)	(0.10)	(0.08)	(0.10)	(0.01)
D2	0.0126	0.0225	0.00894	0.00975	0.0153	0.0107	0.0138	0.0163
	(0.13)	(0.12)	(0.14)	(0.70)	(0.21)	(0.18)	(0.21)	(0.02)
D3	5.34	5.92	6.99	9.57	9.84	11.3	7.84	9.75
	(0.09)	(0.09)	(0.13)	(0.21)	(0.10)	(0.07)	(0.06)	(0.12)
D4	3.68	3.76	3.48	3.35	3.16	3.07	3.52	3.23
	(0.01)	(0.01)	(0.03)	(0.02)	(0.01)	(0.01)	(0.02)	(0.01)
D5	0.0235	0.0361	0.0171	0.0149	0.0266	0.0206	0.0268	0.0271
	(0.11)	(0.08)	(0.23)	(0.38)	(0.10)	(0.08)	(0.11)	(0.01)
D6	1.18	0.99	0.954	0.58	1.13	0.877	1.06	0.72
	(0.38)	(0.35)	(0.40)	(0.60)	(0.37)	(0.40)	(0.43)	(0.29)
D7	0.754	0.76	0.798	0.851	0.814	0.848	0.787	0.835
	(0.05)	(0.05)	(0.04)	(0.06)	(0.03)	(0.02)	(0.04)	(0.03)
D8	0.0602	0.0598	0.0732	0.135	0.178	0.246	0.121	0.247
	(0.09)	(0.12)	(0.08)	(0.08)	(0.07)	(0.04)	(0.08)	(0.04)
D9	0.972	0.94	0.983	0.978	0.965	0.979	0.97	0.961
	(0.01)	(0.02)	(0.01)	(0.02)	(0.02)	(0.01)	(0.01)	(0.01)
D10	0.872	0.75	0.925	0.908	0.848	0.91	0.871	0.838
	(0.02)	(0.05)	(0.01)	(0.07)	(0.03)	(0.02)	(0.03)	(0.01)

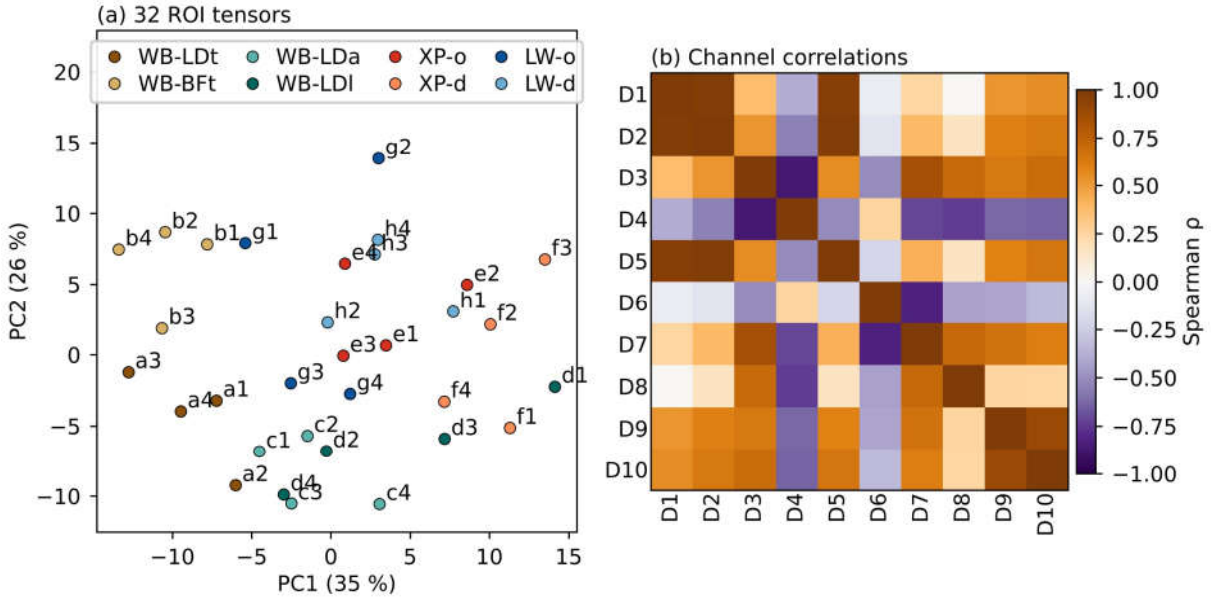


Figure 10. (a) Projection of the 32 ROI tensors (160 entries each; D1, D2 and D5 log-transformed; each entry standardised across ROIs) on the first two principal components; labels: panel letter (Figure 2) and ROI number. (b) Spearman rank correlations between the ten channels over the 512 entries of the eight R = 4 tensors.

Interpretation. The gradient channels are again nearly collinear (Spearman ρ(D1,D2) = 0.98, ρ(D1,D5) = 0.96, ρ(D2,D5) = 0.98), as in human, fish and guppy muscle (Ţălu, 2026c, 2027a), so one of them can represent the group. Contrast and correlation are only weakly related (ρ(D6,D9) = −0.42), as on human and fish muscle and unlike synthetic textures, because the variance of the quantised image changes between panels and scales. The longitudinal section has the largest modulation of the gradient channels (D2: 0.70), and the near-isotropy of LW-d appears in every directional channel (D1, D2, D5 ≤ 0.02). In the principal-component projection (PC1 35 %, PC2 26 % of the variance) the ROIs group by panel and the wild boar ROIs lie apart from most domestic pig ROIs,

but magnification, staining and laboratory differ between the two sources, so this separation cannot be attributed to the animals.

Discussion. The three new results answer the question left open by the earlier applications of the tensor: what an anisotropy value is made of. Proposition 1 shows that *A* is the product of local order and alignment, which trade off with the integration window; the crossover scale ρ_c adds an orientation-domain size to *A*, and it distinguished sections in which orientation changes from fibre to fibre (wild boar transverse, $\rho_c \approx 7–12$ μm), from fascicle to fascicle (domestic pig, 42–87 μm), or not at all (longitudinal, 2.9 μm). Proposition 2 extends the equal-area pooling inequality to compartments of any size and shows that a section can look isotropic because its oriented components cancel. Proposition 3 gives the anisotropy that fibre shape alone can produce, so that the remaining anisotropy can be attributed to the connective tissue. Together they turn *A* from a single number into a decomposition by component and scale.

Applied to porcine muscle, the decomposition shows that directional organisation in transverse H&E sections is carried by the connective-tissue boundaries, which hold 83–93 % of the gradient energy. At fibre level, in fields without wide septa, *A* is approximately accounted for by the moderate elongation and partial alignment of fibre profiles, as Proposition 3 predicts. At fascicle level the perimysium dominates: the straight, roughly parallel septa of the Large White overview give an anisotropy that increases with scale up to 22 μm, whereas the branching septa of the Xiang overview give an anisotropy that falls to 0.07 at that scale. Perimysial architecture is a recognised determinant of the background toughness of meat (Purslow, 2005; Nishimura, 2010), and the scale-resolved anisotropy is a segmentation-free descriptor of it, which the septal energy share, obtained from a threshold-based partition, complements. The compartment analysis of the Large White detail field shows why a single anisotropy value can be misleading: endomysial lines perpendicular to a septum reduce *A* by 90 %, although both components are clearly oriented.

The tensor readings are broadly consistent with the morphometry of the source study. The median minor-axis lengths of the segmented fibres in the Xiang detail field (42.4 μm) and the Large White overview (61.6 μm) are close to the reported diameters (about 40 and 61 μm), whereas the other two fields gave 53.5 and 53.3 μm, so the agreement depends on the field and magnification; field selection, local variability and segmentation may all contribute, and the comparison is not a validation of the calibration. The "oval" and "irregularly square" profile shapes of the two breeds appear as a difference in circularity at equal elongation. The characteristic scale of Xiang muscle was reproduced across a 2.5-fold change of magnification, which supports reading it as a tissue property where the dominant structure is the same in both fields; that of Large White muscle was not (15.9 and 5.2 μm), because the two fields are dominated by different structures (Table 8). These agreements concern single published fields. They show that the measurements are consistent; they are not evidence of breed differences, for which several animals and fields per breed are required.

Intramuscular fat was expected to dilute anisotropy, and Proposition 2 states precisely when it does: only when the adipocytes form an isotropic compartment with a substantial share of the gradient energy. The wild boar adipocyte field did not satisfy this condition. Two large adipocytes carried 13 % of the energy and were themselves oriented, and the quadrant containing most of the adipocyte area was the most anisotropic. The higher intramuscular fat of Xiang pigs (5.65 % against 2.43 %) is not visible as adipocytes in the analysed fields. The effect of marbling on *A* therefore remains a hypothesis that Eq. (8) makes testable on sections with many small adipocytes.

Compared with the human and fish muscle sections analysed earlier, the porcine transverse sections, except the nearly isotropic Large White detail field, have similar anisotropy at fibre level ($A = 0.13–0.26$ against 0.21 and 0.39). The same collinearity of the gradient channels, the same decoupling of co-occurrence contrast and correlation and the same dependence of the isotropic floor on ROI size were found. The longitudinal wild boar section provides a reference that was missing in the earlier studies: real tissue with

a known fibre direction, which the tensor recovered (axis 90.8°, CI 87.5–94.2°) with A = 0.697.

Limitations. Eight published panels from two laboratories were analysed: one field per specimen, with unknown compression, staining protocol and processing history, so differences between sources (wild boar versus domestic pig) cannot be separated from technical differences. The wild boar panels are small (213–316 px high), which widens the bootstrap intervals and raises the isotropic floors of the four-ROI configuration. The detail fields of the domestic pig image are magnifications of parts of the overviews and are not independent observations. The morphometry of the wild boar panels rests on only 10–18 complete fibre profiles per panel. Annotations were removed by inpainting (up to 8.2 % of a ROI). Proposition 3 assumes thin edges of uniform contrast and smooth outlines; real fibre profiles are polygonal and their segmentation has its own errors, and the apparent obliquity is only an upper bound. Proposition 1 is exact only under sum-preserving smoothing; on finite ROIs the product deviated from A by up to 7 % (more in the nearly isotropic LW-d field). The compartments were defined by thresholds whose choice (opening radius 5 μm) affects the septal–endomysial split, although the reconstruction of A by Eq. (6) is exact for any partition. The surrogates are Gaussian and the block bootstrap neglects long-range correlation. Next steps are calibrated sections from several animals per breed, field-to-field repeatability, sections with intramuscular adipocytes to test Eq. (8), and comparison with fibre-type histochemistry.

Conclusions. Three results were added to the hierarchical texture-descriptor tensor: an exact factorisation of the anisotropy index into local coherence and alignment of local axes, with a crossover integration scale at which both equal $\sqrt{A}$ (for $0 < A < 1$); an exact decomposition of the anisotropy over tissue compartments of arbitrary area, with a cancellation law for compartments with perpendicular axes and a dilution law for isotropic compartments; and a closed-form law for the anisotropy of elliptical fibre profiles. The law was verified on synthetic ellipses and mosaics within 0.004. Applied to eight calibrated H&E sections of wild boar, Xiang and Large White muscle, the tensor showed that directional organisation is carried by the connective-tissue boundaries. Fibre-profile shape and alignment explained the anisotropy of fields without wide septa, and the perimysial septa dominated at fascicle scale, where the Large White and Xiang overviews differed clearly. The longitudinal section gave the expected fibre direction, and the characteristic scale of Xiang muscle was reproduced across magnifications, but that of Large White muscle was not (15.9 and 5.2 μm). These results provide interpretable readings of porcine muscle architecture, segmentation-free for the tensor itself and segmentation-based for the compartment and fibre-profile analyses; differences between breeds or meat-quality classes require replicated, calibrated material.

Acknowledgement. The author thanks the authors of Odung et al. (2025) and Wang et al. (2024) for publishing their histological images under open licences.

Authors Contributions. Ştefan Ţălu contributed to all aspects of the work.

Conflicts of Interest. The author declares that there is no conflict of interest.

Copyright and Permissions. The panels of Figure 2 and the image backgrounds of Figures 4, 6, 7 and 9 are reproduced and adapted from Odung et al. (2025) (CC BY-SA 4.0) and Wang et al. (2024) (CC BY 4.0); source and licence are stated in each caption. Adapted material from Odung et al. (2025) is shared under CC BY-SA 4.0. All other figures were produced by the author.

Data Availability. The analysis code, ROI coordinates and numerical results supporting the findings of this study are available from the corresponding author upon request.

Use of generative AI. During the preparation of this manuscript, the author used GPT-6 Astra to assist in the preparation of the graphical abstract and a figure. The author reviewed and edited the AI-assisted visual materials as necessary and takes full responsibility for the accuracy, originality, and integrity of all content in the manuscript.

Funding. This research received no external funding.

References

Abramowitz, M., & Stegun, I. A. (1964). *Handbook of mathematical functions with formulas, graphs, and mathematical tables*. National Bureau of Standards, Applied Mathematics Series 55. U.S. Government Printing Office.

Bigün, J., & Granlund, G. H. (1987). Optimal orientation detection of linear symmetry. In *Proceedings of the First International Conference on Computer Vision* (pp. 433–438). London.

Cadar, M. E. (2011). Comparative morphometric analysis of *longissimus dorsi* muscle structure in wild and domestic pigs. Bulletin of University of Agricultural Sciences and Veterinary Medicine Cluj-Napoca. Animal Science and Biotechnologies, 68(1–2). https://doi.org/10.15835/buasvmcn-asb:68:1-2:6676

Depeursinge, A. (2017). Multiscale and multidirectional biomedical texture analysis: Finding the needle in the haystack. In A. Depeursinge, O. S. Al-Kadi, & J. R. Mitchell (Eds.), *Biomedical texture analysis* (pp. 29–53). Academic Press.

Freeman, W. T., & Adelson, E. H. (1991). The design and use of steerable filters. *IEEE Transactions on Pattern Analysis and Machine Intelligence, 13*(9), 891–906. https://doi.org/10.1109/34.93808

Ghalati, M. K., Nunes, A., Ferreira, H., Serranho, P., & Bernardes, R. (2022). Texture analysis and its applications in biomedical imaging: A survey. *IEEE Reviews in Biomedical Engineering, 15*, 222–246. https://doi.org/10.1109/RBME.2021.3115703

Haralick, R. M., Shanmugam, K., & Dinstein, I. (1973). Textural features for image classification. *IEEE Transactions on Systems, Man, and Cybernetics, SMC-3*(6), 610–621. https://doi.org/10.1109/TSMC.1973.4309314

Hocquette, J. F., Gondret, F., Baéza, E., Médale, F., Jurie, C., & Pethick, D. W. (2010). Intramuscular fat content in meat-producing animals: Development, genetic and nutritional control, and identification of putative markers. *Animal, 4*(2), 303–319. https://doi.org/10.1017/S1751731109991091

Joo, S. T., Kim, G. D., Hwang, Y. H., & Ryu, Y. C. (2013). Control of fresh meat quality through manipulation of muscle fiber characteristics. *Meat Science, 95*(4), 828–836. https://doi.org/10.1016/j.meatsci.2013.04.044

Karlsson, A. H., Klont, R. E., & Fernandez, X. (1999). Skeletal muscle fibres as factors for pork quality. *Livestock Production Science, 60*(2–3), 255–269. https://doi.org/10.1016/S0301-6226(99)00098-6

Künsch, H. R. (1989). The jackknife and the bootstrap for general stationary observations. *The Annals of Statistics, 17*(3), 1217–1241. https://doi.org/10.1214/aos/1176347265

Lefaucheur, L. (2010). A second look into fibre typing – Relation to meat quality. *Meat Science, 84*(2), 257–270. https://doi.org/10.1016/j.meatsci.2009.05.004

Lindeberg, T. (1998). Feature detection with automatic scale selection. *International Journal of Computer Vision, 30*(2), 79–116. https://doi.org/10.1023/A:1008045108935

Mardia, K. V., & Jupp, P. E. (2000). *Directional statistics*. John Wiley & Sons.

Nishimura, T. (2010). The role of intramuscular connective tissue in meat texture. *Animal Science Journal, 81*(1), 21–27. https://doi.org/10.1111/j.1740-0929.2009.00696.x

Odung, E. M., Maha, I. T., Nitbani, H., Jacob, J. M., Amalo, F. A., & Selan, Y. N. (2025). Anatomical and histological features in muscles of wild boar (*Sus scrofa*) from Timor Island. *Acta Veterinaria Indonesiana*, *13*(2), 133–140.

Otsu, N. (1979). A threshold selection method from gray-level histograms. *IEEE Transactions on Systems, Man, and Cybernetics, 9*(1), 62–66. https://doi.org/10.1109/TSMC.1979.4310076

Petrescu-Mag, I. V., Ţălu, Ş., & Şahin, D. (2026). Fractal, multifractal and entropy-based approaches in aquaculture: An integrative review. *Aquaculture, Aquarium, Conservation & Legislation, 19*(2), 882–898.

Purslow, P. P. (2005). Intramuscular connective tissue and its role in meat quality. *Meat Science, 70*(3), 435–447. https://doi.org/10.1016/j.meatsci.2004.06.028

Rehfeldt, C., Fiedler, I., Dietl, G., & Ender, K. (2000). Myogenesis and postnatal skeletal muscle cell growth as influenced by selection. *Livestock Production Science, 66*(2), 177–188. https://doi.org/10.1016/S0301-6226(00)00225-6

Ruusunen, M., & Puolanne, E. (2004). Histochemical properties of fibre types in muscles of wild and domestic pigs and the effect of growth rate on muscle fibre properties. *Meat Science, 67*(3), 533–539. https://doi.org/10.1016/j.meatsci.2003.12.008

Ryu, Y. C., & Kim, B. C. (2005). The relationship between muscle fiber characteristics, postmortem metabolic rate, and meat quality of pig *longissimus dorsi* muscle. Meat Science, 71(2), 351–357. https://doi.org/10.1016/j.meatsci.2005.04.015

Telea, A. (2004). An image inpainting technique based on the fast marching method. *Journal of Graphics Tools, 9*(1), 23–34. https://doi.org/10.1080/10867651.2004.10487596

Theiler, J., Eubank, S., Longtin, A., Galdrikian, B., & Farmer, J. D. (1992). Testing for nonlinearity in time series: The method of surrogate data. *Physica D, 58*(1–4), 77–94. https://doi.org/10.1016/0167-2789(92)90102-S

Ţălu, Ş. (2012a). Mathematical methods used in monofractal and multifractal analysis for the processing of biological and medical data and images. *Animal Biology & Animal Husbandry, 4*(1), 1–4.

Ţălu, Ş. (2012b). Texture analysis methods for the characterisation of biological and medical images. *Extreme Life, Biospeology & Astrobiology, 4*(1), 8–12.

Ţălu, Ş. (2013a). Characterization of retinal vessel networks in human retinal imagery using quantitative descriptors. *Human & Veterinary Medicine, 5*(2), 52–57.

Ţălu, Ş. (2013b). Multifractal geometry in analysis and processing of digital retinal photographs for early diagnosis of human diabetic macular edema. *Current Eye Research, 38*(7), 781–792. https://doi.org/10.3109/02713683.2013.779722

Ţălu, Ş. (2026a). A multidimensional implementation lattice for translational human and veterinary medicine. *Human & Veterinary Medicine, 18*(1), 9–23.

Ţălu, Ş. (2026b). A unified fractal-entropy-manifold framework for multi-modal medical image fusion. *Human & Veterinary Medicine, 18*(1), 40–52.

Ţălu, Ş. (2026c). Application of the hierarchical texture-descriptor tensor to histological muscle sections of *Poecilia reticulata*. *Poeciliid Research, 16*(1), 62-74. https://doi.org/10.67784/0096

Ţălu, Ş. (2027a). A hierarchical tensor framework for quantitative multiscale and multidirectional biomedical texture characterization. *Human & Veterinary Medicine, 19*(1), 32-53. https://doi.org/10.67784/0095

Ţălu, Ş. (2027b). Descriptor-tensor texture analysis of myostatin-edited rabbit muscle: A two-study replication. *Rabbit Genetics, 17*(1). https://doi.org/10.67784/0097

Ţălu, Ş. (2027c). Scale and orientation signatures of soil structure in thin sections: A hierarchical descriptor tensor applied to greenhouse soils under conventional, pollution-free and organic management. *Advances in Environmental Sciences, 19*(1). https://doi.org/10.67784/0099

Ţălu, Ş., & Giovanzana, S. (2011). Fractal and multifractal analysis of human retinal vascular network: A review. *Human & Veterinary Medicine, 3*(3), 205–212.

Ţălu, Ş., & Giovanzana, S. (2012). Image analysis of the normal human retinal vasculature using fractal geometry. *Human & Veterinary Medicine, 4*(1), 14–18.

Ţălu, Ş., Stach, S., Sueiras, V., & Ziebarth, N. M. (2015). Fractal analysis of AFM images of the surface of Bowman's membrane of the human cornea. *Annals of Biomedical Engineering, 43*(4), 906–916. https://doi.org/10.1007/s10439-014-1140-3

Ţălu, Ş., Vlăduţiu, C., Popescu, L. A., Lupaşcu, C. A., Vesa, Ş. C., & Ţălu, S. D. (2013). Fractal and lacunarity analysis of human retinal vessel arborisation in normal and amblyopic eyes. *Human & Veterinary Medicine, 5*(2), 45–51.

Vincent, L., & Soille, P. (1991). Watersheds in digital spaces: An efficient algorithm based on immersion simulations. *IEEE Transactions on Pattern Analysis and Machine Intelligence, 13*(6), 583–598. https://doi.org/10.1109/34.87344

Wang, W., Wang, D., Zhang, X., Liu, X., Niu, X., Li, S., Huang, S., Ran, X., & Wang, J. (2024). Comparative transcriptome analysis of *longissimus dorsi* muscle reveal potential genes affecting meat trait in Chinese indigenous Xiang pig. *Scientific Reports*, *14*, 8486. https://doi.org/10.1038/s41598-024-58971-2

Received: 13 September 2026. Accepted: 31 October 2026. Published online: 31 October 2026.
Author:
Ştefan Ţălu, The Directorate of Research, Development and Innovation Management (DMCDI), The Technical University of Cluj-Napoca, Constantin Daicoviciu St., no. 15, Cluj-Napoca 400020, Cluj County, Romania, e-mail: stefan.talu@auto.utcluj.ro; stefan.talu1@gmail.com https://orcid.org/0000-0003-1311-7657
This is an open-access article distributed under the terms of the Creative Commons Attribution License (CC-BY 4.0), which permits unrestricted use, distribution and reproduction in any medium, provided the original author and source are credited.
How to cite this article:
Ţălu, Ş. (2027). Coherence, alignment and fibre-profile geometry in a hierarchical texture-descriptor tensor: Application to H&E sections of skeletal muscle in wild boar (*Sus scrofa*) and domestic pigs. *Porcine Research, 17*(1), 1–22. https://doi.org/10.67784/0098